CHEMISTRY OF MATERIALS
Cite This: Chem. Mater. 2019, 31, 4793−4804
Article
pubs.acs.org/cm

Integrated Isothermal Atomic Layer Deposition/Atomic Layer Etching Supercycles for Area-Selective Deposition of TiO_2

Seung Keun Song, Holger Saare, and Gregory N. Parsons*

Department of Chemical and Biomolecular Engineering, North Carolina State University, Raleigh, North Carolina 27695, United States

Supporting Information

ABSTRACT: New approaches for area-selective deposition (ASD) are becoming critical for advanced semiconductor patterning. Atomic layer deposition (ALD) and atomic layer etching (ALE), that is, "inverse ALD", are considered important for ASD, but to date, direct integration of ALD and ALE for ASD has not been reported. This work demonstrates that self-limiting thermally driven ALE, using WF_6 and BCl_3, can be directly coupled with self-limiting thermal ALD, using $TiCl_4$ and H_2O, in a single isothermal reactor at temperature <200 °C to achieve ASD of TiO_2 thin films on common Si/SiO_2-patterned surfaces without the use of organic nucleation inhibitors. We show that ALD/ALE "supercycles" (where one supercycle comprises, e.g., 30 ALD cycles followed by 5 ALE cycles) can be reliably repeated to yield more than 12 nm of TiO_2 while maintaining a selectivity fraction $S > 0.9$, nearly a 10× improvement over previous reports of inherent TiO_2 ASD. After ALD/ALE (=30/5) 14 supercycles at 170 °C, X-ray photoelectron spectroscopy data show a small Ti 2p signal on Si−H (hydrogen fluoride-cleaned Si), with no Ti 2p signal detected after additional "postetch" ALE cycles. At 150 °C, extended supercycles lead to unwanted particles visible by electron microscopy, which is ascribed to the formation of unreactive mixed silicon/titanium oxide nuclei. The number density of visible particles is consistent with modeled film growth trends. Overall, this work provides new insights into the capabilities for ASD of dielectric materials and a starting point to realize more complex atomic-scale processes using ALD, ALE, and other self-limiting reaction schemes.

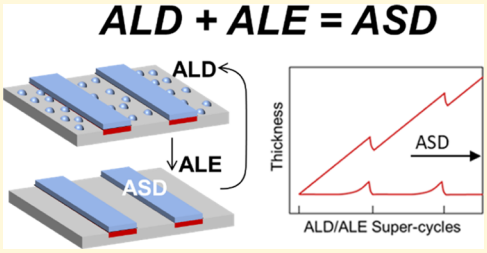

INTRODUCTION

To pattern features with sub-10 nm resolution in semiconductor devices, significant research effort is now being focused into area-selective deposition (ASD), where a thin film material is deposited in a desired "growth" region while minimizing deposition in the adjacent "nongrowth" regions on a starting substrate surface. Processes including thermally driven chemical vapor deposition (CVD)[1,2] and plasma-enhanced or thermal atomic layer deposition (ALD)[3−19] are commonly studied for this purpose. Area-selective epitaxial CVD of silicon/germanium is known in semiconductor device manufacturing, but it requires temperatures exceeding 700 °C,[1] making it unsuitable for "back-end" fabrication where temperatures <400 °C are required.[20] Area-selective CVD of cobalt capping layers on copper interconnects is also known to be useful,[2] but it is limited to ∼10 nm of deposition before selectivity is degraded.

Many approaches to area-selective ALD (AS-ALD) have been demonstrated, including inherent surface-dependent ALD nucleation,[12−15,18,19] surface passivation using polymers or molecules,[3−6] and local nucleation activation.[16] Researchers are also beginning to explore combining ALD with traditional wet chemical[4,7] or plasma-based[17] etching reactions to remove unwanted nuclei from the nongrowth surface. For ASD of TiO_2, Ti precursors including titanium tetrachloride,[12,18,19,21−27] titanium isopropoxide,[25,28−35] alkyl-amino titanium,[14,36,37] and titanium methoxide[38,39] have been studied. McDonnell et al.[18] compared TiO_2 ALD using $TiCl_4/H_2O$ on oxidized and hydrogen-terminated Si(111) and Si(100) and found that 1−2 nm of TiO_2 could be achieved on oxidized silicon with minimal deposition (2−6 at. % of Ti) on Si−H. Furthermore, by locally removing hydrogen using scanning tunneling microscopy tip-based lithography, they showed selective deposition of TiO_2 lines ∼2.8 nm tall and 18 nm wide on bare silicon versus Si−H. Further work from Longo et al.[12] confirmed that inherent selectivity results from the thermodynamically favorable adsorption of $TiCl_4$ on Si−OH versus unfavorable adsorption on Si−H. Blocking layers, including polymer thin films and resists[24−26,28,36] (i.e., for patterning via "lift-off"), and self-assembled monolayers (SAMs)[23,29−31] have also been studied for TiO_2 ASD. Hashemi et al.[31] reported that alkanethiol SAMs allowed up to 12 nm of TiO_2 on blanket silicon before Ti signal was detected by X-ray photoelectron spectroscopy (XPS) on the SAM. In another report using perfluorodecyl-trichlorosilane blocking layers during TiO_2 CVD under low-flux conditions, patterned films exceeding 90 nm were achieved.[33] Vallat et al.[40] studied AS-ALD of TiO_2 by incorporating periodic NF_3

Received: March 21, 2019
Revised: May 21, 2019
Published: June 12, 2019

DOI: 10.1021/acs.chemmater.9b01143
Chem. Mater. 2019, 31, 4793−4804

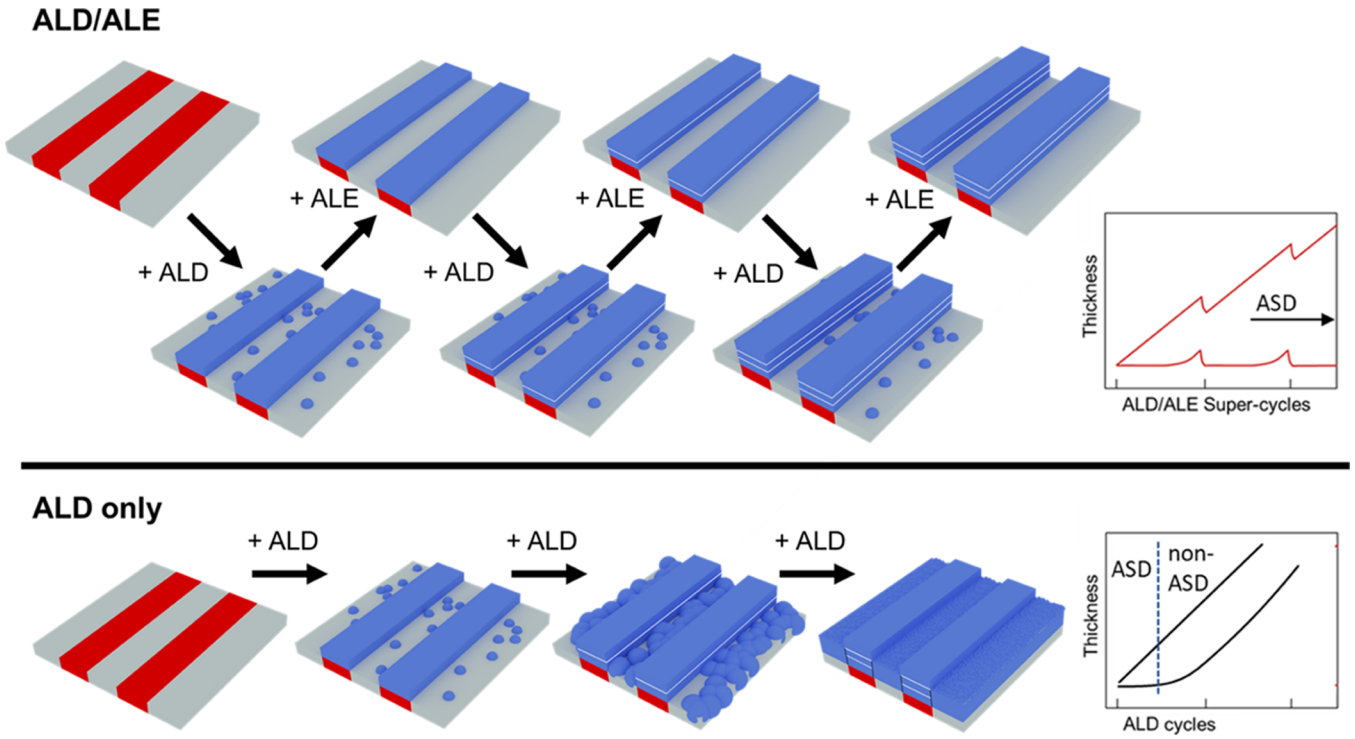

Figure 1. Schematic of the fully integrated ALD/ALE process sequence, including the possible thickness evolution on different substrates after multiple ALD/ALE supercycles (top). In comparison to the ALD/ALE process, the possible thickness evolution on different substrates after multiple ALD cycles is also shown (bottom).

plasma exposure steps into a TiO_2 plasma-enhanced ALD process. The approach led to 11 nm of TiO_2 on TiN with minimal deposition on SiO_2, but the intermittent plasma exposure appeared to modify the crystallinity of deposited TiO_2. Despite this recent progress, only a small number of studies have reported the quantitative analysis of selectivity[8,11] to allow direct comparison between different data sets. More analysis is needed to understand the limits of ASD and to understand the mechanisms associated with unwanted material nucleation and the associated mechanisms leading to selectivity loss.

Compared to conventional plasma etching, self-limiting atomic layer etching (ALE) provides finer etch control, making it a critical emerging technology for nanoscale device engineering.[41,42] Ion- or plasma-enhanced ALE involves a self-limiting surface conversion reaction producing a chemically labile product, followed by the removal of the labile surface layer via energetically enhanced ions or radicals.[41−45] Beyond plasma-based etching, there is also interest in thermal-based ALE[46−52] using sequential self-limiting surface reactions to achieve "inverse ALD."

Over the past few years, several authors have suggested coupling ALD with ALE to create new "atomic scale processes,"[20,53,54] but results demonstrating feasibility, benefits, and challenges of integrated ALD and ALE have not been reported so far. This work demonstrates for the first time that thermal ALD and thermal ALE can be successfully integrated under low-temperature isothermal conditions in a single vapor-phase reactor to achieve highly selective deposition. We choose TiO_2 as a sample system and show a selectivity fraction $S > 0.9$ with thickness > 12 nm on common patterned Si/SiO_2 surfaces, without the need for blocking layers or other nucleation inhibitors.

The selectivity fraction is defined as $S = (\theta_1 - \theta_2)/(\theta_1 + \theta_2)$ where θ_1 and θ_2 are the measured or calculated surface coverage on the desired growth and nongrowth surfaces, respectively.[8] This definition allows quantitative comparison of different ASD processes.[8] For example, in this article, we determine and compare values for $t_{S=0.9}$, the thickness of TiO_2 in the desired growth region when $S = 0.9$, for ALD versus ALD/ALE processes.

Figure 1 presents a schematic for TiO_2 nucleation and ASD using ALD/ALE "supercycles" compared with the previous ALD-only approach. One ALD/ALE supercycle generally consists of several ALD cycles (e.g., 30) followed immediately by several (e.g., 5) ALE cycles in the same reaction chamber at the same reaction temperature. We tested a range of ALD and ALE cycle numbers and cycle ratios, and conditions showing reasonable results were used for more detailed studies, without further optimization. For this work, TiO_2 was selected as a demonstration material because the ALD process using $TiCl_4$ and H_2O is well developed,[55−57] and a thermal ALE process is available and quantified in our laboratory.[50] The Si−OH/Si−H substrate pair was selected because the materials are commonly available and are known to show a substantial difference in the initial TiO_2 nucleation. We also describe opportunities to extend this approach to other deposition materials and substrates.

Results shown here demonstrate that direct isothermal coupling of thermal TiO_2 ALD and thermal TiO_2 ALE[50] can systematically and controllably remove unwanted TiO_2 nuclei to achieve ASD. Beyond demonstrating capability for ASD, this work also uses in situ reaction analysis to explore mechanisms that are unique to integrated ALD/ALE, including how ALD and ALE reactions proceed at the transition from ALD to ALE and from ALE to ALD, and the stability and repeatability of

DOI: 10.1021/acs.chemmater.9b01143
Chem. Mater. 2019, 31, 4793−4804

multiple ALD/ALE supercycle sequences. Furthermore, by extending the ALD/ALE sequence to thicker film deposition, we systematically examine mechanisms associated with unwanted nuclei generation and associated degradation and loss of selectivity and identify possible means to improve the selectivity fraction and deposition thickness beyond that shown here.

EXPERIMENTAL SECTION

TiO_2 ALD and ALE Reaction Conditions. The ALD and ALE reactions were conducted in a custom-built tubular hot-walled isothermal viscous-flow ALD reactor system described previously[50] under constant temperature (150−190 °C) and pressure (900 mTorr) conditions. TiO_2 ALD films were deposited using 99% pure $TiCl_4$ (Strem Chemicals) and deionized (DI) water as reactants, with ALD dosing sequence (i.e., one ALD cycle) = $TiCl_4/N_2/H_2O/N_2$ = 0.1/45/0.1/45 s, respectively. The purge gas was 99.999% pure N_2 (Arc3 Gases). Consistent with previous results,[19,58,59] between 150 and 190 °C, these dosing conditions show ALD growth saturation, and the slope of the thickness versus cycle plot gives a constant growth rate of ∼0.038 nm/cycle on Si−OH substrates at 170 °C, whereas 150 °C shows ∼0.041 nm/cycle of growth rate on Si−OH.

Self-limiting thermally driven ALE of TiO_2 was carried out using a previously described method using sequential exposures of 99.99% pure WF_6 (Galaxy Chemical) and 99.9% pure BCl_3 (Matheson) at temperatures between 150 and 190 °C.[50] The reactant dose/purge sequence followed $WF_6/N_2/BCl_3/N_2$ with cycle times (i.e., one ALE cycle) of 0.1/45/1.0/45 s, respectively. Under these dosing conditions, the steady-state etch rate of TiO_2 is approximately −0.07 nm/cycle at 170 °C, with decreasing etch rate at lower temperatures.[50]

Quartz Crystal Microbalance. Mass gain and loss during ALD and ALE were monitored using an in situ quartz crystal microbalance (QCM) at reactor temperatures of 150, 170, and 190 °C and fixed dose sequence times. For these tests, a QCM probe body (Kurt Lesker) configured with a 6 MHz gold-coated crystal sensor (Inficon) was inserted into the reactor and allowed to stabilize at the reaction temperature under a steady N_2 flow for at least 120 min. The QCM sensor probe was configured with back-side N_2 purge to avoid deposition on the exposed electrical contacts. Typically, fresh QCM Au crystals were treated with ∼200 ALD cycles of TiO_2. In situ mass change (ng/cm^2) data was collected via electronic data acquisition.

Substrate Preparation. Silicon wafers with hydroxylated chemical SiO_2, referred to as SiO_2 or Si−OH, were prepared using boron-doped Si(100) with 5−10 Ω cm resistivity. The wafers were cut into small pieces (1.3 cm × 1.3 cm) and cleaned by piranha solution (H_2O_2/H_2SO_4 = 1:1 volume ratio) for 15 min. Oxidized pieces were then rinsed with DI water and stored in a DI water-filled vial. The prepared Si−OH was rinsed with DI water and dried with N_2 right before loading it to the reactor. After preparation, ellipsometry indicated a chemical oxide layer of ∼2 nm on the surface and a water contact angle showing a near perfect wetting (≈0°). These prepared Si−OH samples remained stable in laboratory storage for several weeks.

Hydrogen-terminated silicon (Si−H) was prepared by dipping the prepared Si−OH into 5% aqueous hydrogen fluoride (HF) solution for 30 s, followed by washing with DI water for 30 s and drying with flowing N_2. Ellipsometry analysis showed thin nonuniform patches (<0.5 nm) of oxide on Si−H, and the water contact angle was always >70° and typically near 80°. To minimize surface oxidation and contamination, the Si−H substrates were always loaded into the reactor within 10 min after HF treatment.

Patterned Si/SiO_2 wafers were prepared by photolithographic wet-etching of thermally oxidized silicon wafers. The pattern consisted of long (>1 cm) SiO_2 lines separated by exposed substrate silicon. The SiO_2 line width and line spacing were both about 3 μm. The thickness of the SiO_2 layer was approximately 100 nm, although some variation in the feature height and width were observed for samples prepared in different batches. Before placing Si/SiO_2-patterned substrates into the reactor, the samples were cleaved into small pieces (1.3 cm × 1.3 cm), sequentially cleaned using piranha solution for removing contaminants from the surfaces, and etched by 5% aqueous HF solution for 30 s to remove native oxide from the Si surfaces.

For infrared (IR) analysis, high-surface-area porous silicon substrates (porous-Si−H and porous-Si−OH) were prepared by electrochemical etching of double-sided polished silicon [boron-doped Si(100) with 30−60 Ω cm resistivity].[60,61] The wafers were cut into 4.5 cm × 4.5 cm pieces and then cleaned by piranha solution, as mentioned above. To form the silicon anode, a piece of aluminum foil was adhered to a Teflon disk using a polyimide tape, and the clean silicon wafer was placed onto the aluminum foil. A rubber ring and a Teflon ring were then placed on the silicon and clamped to the bottom disk to make a solution-tight seal. Etch solutions comprising 11 mL of 200-proof ethanol anhydrous (Koptec) and 50% HF (Fisher) were sequentially poured into the cylindrical Teflon cell with the silicon wafer exposed, and a Pt coil counter electrode was placed into the etch solution. Electrical current (101 mA, 40 V) was applied across the electrodes by a source meter (Keithley 2606) to initiate chemical surface etching. After about 2 h, the silicon surface appeared blackened, and the electrochemical etched porous silicon was removed from the etch bath and cleaned using DI water, followed by drying under a N_2 flow. Some of the porous silicon samples were subsequently oxidized in piranha solution (following the procedure described above for Si−OH preparation) to create porous-Si−OH samples. Likewise, some porous silicon samples were etched in 5% HF to form porous Si−H.

For all substrates studied, after preparation, the samples were loaded into the ALD/ALE reactor and allowed to stabilize at the reactor temperature for ∼90 min under a N_2 flow before beginning the ALD/ALE processing.

Thickness and Surface Characterization. After TiO_2 ALD or ALD/ALE on Si−H and Si−OH substrates, ex situ spectroscopic ellipsometry was performed (alpha-SE ellipsometer, J.A. Woollam) at 70° incident angle condition to analyze the film thickness. Measured raw data was converted to the film thickness using a Cauchy model available in the ellipsometry software package. The thickness reported is the average of three values measured at different points on each sample. The thickness variation on each sample was typically ± a few percent.

To observe the TiO_2 film thickness change on Si−OH and Si−H during ALD/ALE, a few measurements were made using in situ ellipsometry characterization. A four-wavelength ellipsometer (FS-1, Film Sense) at 65° incident angle condition was integrated into a warm-wall (100 °C) reactor configuration with Si−H or Si−OH substrates heated to 150 °C. Thickness data was collected from each surface during ALD/ALE = 30/7 cycles, respectively. The dose times were 0.15 s for $TiCl_4$, 0.2 s for H_2O, 0.1 s for WF_6, and 0.1 s for BCl_3. Pure N_2 (99.999%) was used as the carrier gas. Between reactant doses, the reactor purge consisted of a 15 s N_2 flow, 10 s reactor pump-out, and 15 s N_2 flow. The reactor was evacuated using a combination of a rotary vane and a turbomolecular pump. The process was carried out at 600 mTorr pressure.

Angled- and top-view images of blanket and patterned samples were obtained using field emission scanning electron microscopy (SEM, FEI Verios 460L), typically operated at 30° tilt angle, 10 kV, and 0.4 nA conditions. The samples were imaged as prepared, without any metal sputter coating. Transmission electron microscopy (TEM) images were obtained on a JEOL 2100 LAB6 microscope at an accelerating voltage of 200 kV with an Orius CCD camera. Atomic scale selectivity and surface modification of the processed blanket substrates were characterized by ex situ XPS (SPECS XPS system with a PHOIBOS 150 analyzer) using a Mg 300 W source. The analysis included survey scans and high-resolution scans for each component of interest, for example, B, C, O, Si, F, Ti, W, and Cl. Peak positions were calibrated by referencing the adventitious C 1s peak to 284.8 eV.[62] The atomic percentage of each component for each sample was also calculated from the high-resolution peaks using relative sensitivity factors. All XPS raw data were processed with CASA XPS software. The surface morphology of TiO_2 films was

DOI: 10.1021/acs.chemmater.9b01143
Chem. Mater. 2019, 31, 4793−4804

scanned on a 1 μm × 1 μm scale by an atomic force microscope (Dimension 3000 scanning probe microscope, Veeco Digital Instrument), and data processing was conducted with Gwyddion software. Elemental distribution on processed Si/SiO_2 was characterized by time-of-flight secondary ion mass spectroscopy (TOF-SIMS) using a TOF-SIMS V instrument (ION TOF, Inc. Chestnut Ridge, NY).

RESULTS AND DISCUSSION

TiO_2 ALE. To couple two separate ALD and ALE processes at a single reactor temperature, we identified a range of temperatures, between 150 and 190 °C, which is compatible with both processes. At this relatively low temperature, the thin ALD TiO_2 films formed here are expected to remain amorphous.[22,55,63] Self-limiting thermally-driven ALE of TiO_2 was carried out using sequential exposures of WF_6 and BCl_3 at temperatures between 150 and 190 °C,[50] following the A/B reaction sequence

$$\text{A: } 2WF_{6(g)} + 3TiO_{2(s)} \rightarrow 2WO_{3(s)} + 3TiF_{4(g)}$$

$$\text{A}': WF_{6(g)} + B_2O_{3(s)} \rightarrow 2BF_{3(g)} + WO_{3(s)}$$

$$\text{B: } 4BCl_{3(g)} + 3WO_{3(s)} \rightarrow 2B_2O_{3(s)} + 3WOCl_{4(g)}$$

Step A fluorinates TiO_2, forming volatile TiF_4 and solid WO_3, and step B volatilizes WO_3 by ligand exchange to form $WOCl_{4(g)}$ and $B_2O_{3(s)}$. The next WF_6 exposure repeats the TiO_2 surface fluorination (step A) and also volatilizes $B_2O_{3(s)}$ (shown as step A′) by forming $BF_{3(g)}$. Step A is also expected to produce mixed W/Ti oxy-fluorides on the surface, which are subsequently removed (as $TiCl_4$, $WOCl_2$, and BF_3 gases) during step B.[50] For simplicity, the mixed oxy-fluoride species are not shown here. Each of these half-reactions is self-limiting and thermodynamically favorable over 150−190 °C.[50] The reactant dose/purge sequence followed $WF_6/N_2/BCl_3/N_2$ with cycle times (i.e., one ALE cycle) of 0.1/45/1.0/45 s, respectively, producing a steady-state TiO_2 etch rate of −0.07 nm/cycle at 170 °C. As discussed below, it is important to note that during any ALD/ALE supercycle, the amount of material etched during the first ALE cycle is somewhat less than that measured during steady-state saturated ALE,[50] and this rate transition needs to be considered when designing integrated ALD/ALE sequences.

TiO_2 ALD Nucleation and Growth on Si−H and Si−OH. To understand TiO_2 ALD nucleation and to identify the limits of intrinsic ASD of TiO_2 (without integrated etching), we explored TiO_2 ALD on Si−OH and Si−H terminated surfaces over a range of ALD cycles. As a first test, two sample pieces, one with Si−H and one with Si−OH, were placed in the ALD reactor and exposed to TiO_2 ALD at 170 °C for a set number of ALD cycles from 0 to 540. The samples were removed, and the thickness on both samples was measured by ellipsometry, with the results shown in Figure 2a. The thickness on Si−OH grows linearly with the number of ALD cycles. On the Si−H surface, a reaction with the $TiCl_4$ reactant is expected to be thermodynamically unfavorable.[12,18] Consistent with previous reports, the TiO_2 growth on Si−H proceeds slowly after initial nucleation and then accelerates before the nuclei begin to coalesce.[19,64]

Also included in Figure 2a are two solid lines corresponding to a fit to an analytical model for island growth.[8] Using ALD thickness data measured on the desired growth and nongrowth surfaces, a fit to the nucleation model can provide an estimate for the density of nucleation sites present on the starting nongrowth surface, $\hat{N}$ sites·nm^{-2}, and/or the rate of nucleation site generation during the ALD process, $\dot{N}$ sites·nm^{-2}·cycle^{-1} (where $\dot{N} = \dot{N}_0\exp(-\nu_d/\nu)$, $\dot{N}_0$ is the initial generation rate, ν is the cycle number, and ν_d is the characteristic delay in site generation).[8] [Note the distinction between a "nucleation site" and a "nucleus": A nucleation site is a point on the surface that promotes nucleus formation. Nucleation sites (possibly including, but not limited to surface "defect" sites) may be present on the starting surface and/or generated on the surface during deposition and/or etching.[8] Nuclei, on the other hand, consist of material deposited at nucleation sites. For any deposition/etching sequence, the density of nuclei observed experimentally is expected to be related to the density of nucleation sites.] The fit in Figure 2a shows the expected thickness per cycle on Si−OH and Si−H for a growth rate of 0.038 nm cycle^{-1} and a starting nucleation site density of 7 × 10^{-3} sites nm^{-2} on Si−H, indicating that ∼1.9 nm of ASD could be achieved with a selectivity fraction of ∼0.9, that is, $t_{S=0.9} \approx 1.9$ nm.[8]

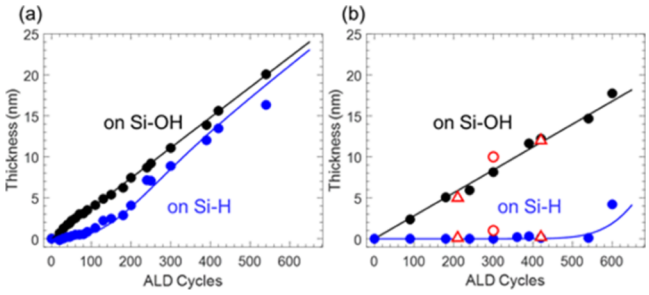

Figure 2. (a) Thickness of TiO_2 ALD at 170 °C on Si−H and Si−OH surfaces measured by ellipsometry as a function of the ALD cycle number. The lines are a fit to the data corresponding to a growth rate of 0.038 nm/cycle with 7 × 10^{-3} nuclei per nm^2 on the starting surface, yielding $t_{S=0.9} \approx 1.9$ nm. (b) Thickness of TiO_2 deposited at 170 °C using coupled ALD/ALE cycles for various number of supercycles: solid dots for ALD/ALE = 30/5 cycles; open circles for ALD/ALE = 50/10; and open triangles for ALD/ALE = 70/15. The thickness vs number of ALD cycles is plotted to allow direct comparison with panel (a). In (b), the lines show the model fit to the (30/5) data, giving $t_{S=0.9} > 15$ nm.

TiO_2 ALD/ALE Supercycles on Blanket Si−H and Si−OH Surfaces. *Ellipsometry.* For integrated ALD and ALE, the number of ALD cycles must be adjusted to produce substantial deposition on Si−OH without excessive deposition on Si−H. Likewise, sufficient ALE is needed to remove nuclei from Si−H and regenerate initial growth delay on Si−H while minimizing the amount etched from the Si−OH surface. Reaction temperature is also an important consideration. The temperature dependence of the ALD and ALE reaction rates indicates that both can operate effectively over a range from about 150°−190 °C. At lower temperatures, the etch rate becomes slower.[50] At T > 190 °C, the TiO_2 ALE sequence transits to a continuous non-self-limiting CVE (chemical vapor etching).[50] Therefore, we examined the integrated ALD/ALE process at 150°, 170°, and 190 °C, with results mostly collected at 170 and 150 °C.

Using Si−H and Si−OH substrates at 170 °C, various combinations of ALD/ALE cycles were evaluated versus number of "supercycles", N, and the thickness on each substrate was measured by ellipsometry. Figure 2b shows the thickness for ALD/ALE = 30/5 cycles, 50/10 cycles, and 70/15 cycles. Using ALD/ALE = 50/10, the results after 6

DOI: 10.1021/acs.chemmater.9b01143
Chem. Mater. 2019, 31, 4793−4804

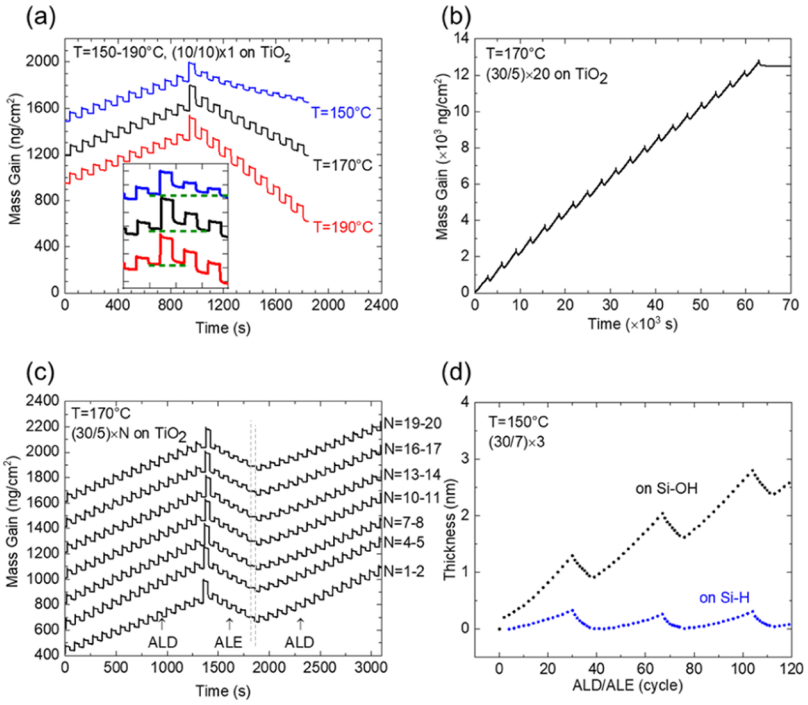

Figure 3. (a) Mass changes during ALD/ALE transition at different temperatures (T = 150, 170, and 190 °C). (b) In situ QCM for (30/5) × 20 at 170 °C on the TiO_2-coated crystal. (c) Overlapped view of mass changes during ALD/ALE/ALD transition at varied supercycles by in situ QCM for (30/5) × 20 at 170 °C on the TiO_2-coated crystal. (d) Magnified view (0−120 total cycles) of in situ ellipsometry-measured TiO_2 thickness for (30/7) at 150 °C on Si−H and Si−OH. Note that QCM (c) and ellipsometry (d) are not compared quantitatively because data was obtained under different conditions in different reactor systems.

supercycles (i.e., a total of 300 ALD cycles) showed ∼1 nm of unwanted TiO_2 on Si−H. For ALD/ALE cycles = 70/15 or 30/5, nearly no growth was observed on Si−H after 420 ALD cycles, indicating that these ratios are preferred over 50/10. The results obtained using different ALD/ALE cycle numbers at 150 and 190 °C showed generally similar trends (Figure S1). Overall, in each supercycle, we sought to keep the number of etch cycles small but sufficient to obtain steady-state etching.[50] Therefore, at 170 °C, the ratio ALD/ALE = 30/5 was selected for a more detailed study. At 150 and 190 °C, results showing good selectivity could also be obtained using different ALD/ALE cycle ratios (Figure S1). At 150 °C, the etch rate is somewhat less, so ALD/ALE = 30/7 was selected because it showed favorable results.

Considering the data for ALD/ALE = 30/5 at 170 °C in Figure 2b, the net TiO_2 growth per cycle on Si−OH is constant at ∼0.83 nm per ALD/ALE supercycle or an average of 0.028 nm per ALD cycle (as discussed below relative to the model fit). As expected, because of etching during the ALE steps, the average thickness per cycle is less than 0.038 nm/cycle, as shown in Figure 2a, where no etching is used. Considering that ∼1 ALE cycle is needed for etch incubation (Figure 3 below), the net deposition of ∼0.83 nm/supercycle obtained using ALD/ALE = 30/5 cycles is consistent with the measured ALD and ALE rates of 0.038 and −0.07 nm/cycle,[50] respectively. A run performed with N = 14 (=420 ALD cycles) shows ∼12 nm of TiO_2 on Si−OH with a negligible ellipsometry signal (<0.2 nm) on Si−H. At N = 18, ∼15 nm of TiO_2 was deposited on Si−OH, also with <0.5 nm on Si−H. However, a run at N = 20 (=600 ALD cycles) yielded several nanometers of TiO_2 on the "nongrowth" Si−H surface, indicating loss of selectivity. Compared to this TiO_2 growth rate of ALD/ALE = 30/5 at 170 °C, the process using 30/7 at 150 °C has a higher growth rate (∼0.92 nm/supercycle) because of an increase in deposition per ALD cycle (∼0.041 nm/cycle) and a decrease in etch per ALE cycle (−0.044 nm/cycle). The higher growth per supercycle on Si−OH, without growth on Si−H, implies that 150 °C may enable better selectivity versus 170 °C.

Model Fit. Figure 2b also shows a fit to the ASD nucleation model[8] for the data collected using ALD/ALE = (30/5) up to N = 20 supercycles. In the model, growth per cycle, $\dot{G}$, is defined as the net average thickness gained on the receptive growth surface per ALD cycle. To analyze data from deposition/etch experiments, the value for $\dot{G}$ (average thickness per ALD cycle) is the net thickness gain per supercycle/number of ALD cycles per supercycle on the receptive growth surface. In Figure 2b, a linear fit to the ALD/ALE = 30/5 cycle data on Si−OH gives $\dot{G}$ = 0.028 nm·cycle^{-1}. For any ASD process, the model fit provides a quantitative measure of selectivity as well as an estimate of the overall number of nucleation sites expected to be present when nuclei are observed (i.e., when selectivity is lost).[8] The fit in Figure 2b for thickness versus ALD cycle on Si−H (obtained using $\dot{G}$ = 0.028 nm·cycle^{-1}, $\dot{N}_0$ = 0.003 nm^{-2}·cycle^{-1}, and ν_d = 4000 cycles) indicates that at 600 ALD cycles (when selectivity is lost), the surface growth is consistent with ∼3 × 10^{-4} nucleation sites/nm^2, increasing during deposition and/or etching as the process proceeds.

In Figure 2b, the abrupt increase in the measured film thickness between 540 (N = 18) and 600 ALD cycles (N = 20) is ascribed to the generation of nucleation sites during the ALD/ALE sequence. For the conditions used, for any $N \leq 18$, the density of nucleation sites is sufficiently small that all nuclei formed during ALD are removed during the ALE cycles. However, as nucleation sites continue to be generated, the

DOI: 10.1021/acs.chemmater.9b01143
Chem. Mater. 2019, 31, 4793−4804

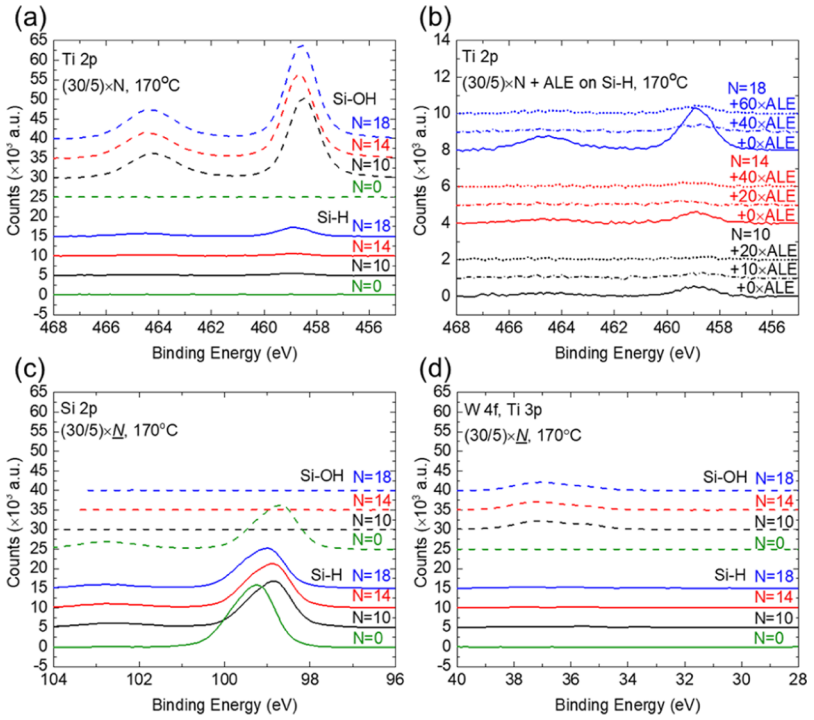

Figure 4. Ex situ XPS data collected from Si−H and Si−OH wafer pieces after ALD/ALE = (30/5) × *N* at 170 °C; high-resolution scan of (a) Ti 2p, (c) Si 2p, and (d) W4f and Ti 3p. (b) XPS Ti 2p for ALD/ALE = (30/5) × *N* with varied additional ALE cycles at 170 °C on Si−H; blue lines for *N* = 18 + ALE (=0, 40, and 60), red lines for *N* = 14 + ALE (=0, 20, and 40), and black lines for *N* = 10 + ALE (=0, 10, 20). The signal observed on Si−OH near 37.2 eV is related to Ti 3p, possibly with a small signal from W 4f at 35.4 eV. Note that the XPS results for samples formed at 150 °C are shown in Figure S6.

fixed number of ALD cycles yields a larger amount of TiO_2. For $N > 18$, the number of nucleation sites is sufficiently large that the amount of film deposited during ALD can no longer be removed during the fixed number of ALE cycles. At this critical point, selectivity is lost and the amount of material deposited per cycle on the original nongrowth surface increases abruptly. Since the nuclei are nonplanar, the slope of the thickness versus cycle data can exceed that measured on the desired growth surface.[8]

The model fit indicates that this process can yield 10 nm of TiO_2 on SiO_2 with selectivity fraction $S > 0.999$ on Si−H. Alternately, the results in Figure 2 show that >15 nm of TiO_2 can be achieved with selectivity fraction $S \geq 0.9$, that is, $t_{S=0.9} >$ 15 nm, compared to $t_{S=0.9} \approx 1.9$ nm using ALD only, nearly a 10× improvement in selectivity. For the fit to the supercycle data in Figure 2b, the observed trend in the thickness versus cycle on Si−H can also be produced using other combinations of $\dot{N}_0$ and ν_d in the model. Whereas the statistical analysis of the fits has not been performed, fits that follow the trend line show good agreement for $t_{S=0.9} > 15$ nm. As described below in the section related to ASD selectivity loss, the mechanism for nucleation site generation is attributed to oxidation of the Si−H surface during the ALD sequence, leading to SiO_2 that is not etched by ALE but is receptive to TiO_2 growth.

In Situ QCM. Results from in situ QCM collected using integrated ALD/ALE are shown in Figure 3. Figure 3a shows the results from QCM at 150, 170, and 190 °C showing the mass increase during ALD followed by mass decrease during ALE. From the slope of the mass uptake trend, the rates of ALD at 150, 170, and 190 °C are nearly the same, but the rate of ALE increases as the reactor temperature increases from 150 to 190 °C.[50] The inset in Figure 3a shows a magnified view of the process transition from ALD to ALE at 150, 170, and 190 °C. For all three temperatures, the first ALE cycle after ALD produces a net mass gain. This gain is ascribed to the uptake of WF_6, forming surface Ti/W oxy-fluorides,[50] leading to incubation for the initiation of net mass loss etching. As shown in the Figure 3a inset, the incubation decreases from ∼3 ALE cycles at 150 °C to ∼1 ALE cycle at 190 °C. At lower temperature, the first WF_6 dose could be less reactive with the ALD TiO_2 surface leading to less surface fluorination and hence less etching. Subsequent WF_6 doses promote fluorination and saturated ALE.

Figure 3b shows the full QCM data trace on a receptive substrate at 170 °C for ALD/ALE = 30/5 cycles over a total of 20 supercycles (i.e., a total of 600 ALD cycles). The zig-zag slope results from the repeated deposition/etch cycles. Figure 3c shows an expanded view of this data, comparing the deposition/etch/deposition transitions at various values of *N* between *N* = 1 and 19. In this plot, the data at *N* = 1 corresponds to the mass change of the first transition during the deposition/etch/deposition sequence, and *N* = 19 is from the near final sequence. During steady-state $TiCl_4/H_2O$ ALD, the $TiCl_4$ dose leads to mass gain and H_2O produces a net mass loss, consistent with the expected $TiCl_4/H_2O$ reaction sequence.[65] However, upon closer examination of the transition from ALE to ALD, we see that the first $TiCl_4$ dose in the ALD sequence leads to no mass change, followed by mass loss during the H_2O step. The negligible mass change during the first $TiCl_4$ dose after ALE suggests that after BCl_3 exposure, the etch surface does not react rapidly with $TiCl_4$ or that the net reaction leads to a balanced mass exchange. Unlike the transition from ALD to ALE, examining the transition from ALE to ALD using QCM at 150 and 170 °C, no noticeable

DOI: 10.1021/acs.chemmater.9b01143
Chem. Mater. 2019, 31, 4793−4804

effect from the reaction temperature was observed (Figure S2). More work is needed to better understand the surface reactions during deposition/etch and etch/deposition transitions.

The data in Figure 3 show excellent repeatability and consistency of the mass change during ALD and ALE over an extended process run time; the total run time for the N = 20 supercycles shown in Figure 3b was ~17.6 h. This data confirms that repeating the ALE steps on the growing TiO_2 surface allows the ALD to proceed for many supercycles before selectivity is eventually lost (vide infra). Figure 3d shows the results from in situ ellipsometry studies of the ALD/ALE sequence on Si−OH and Si−H substrates performed in a different reactor system at T = 150 °C. These data confirm incubation of TiO_2 ALD followed by nuclei removal during ALE on Si−H, with substantial ALD and some ALE on Si−OH. The combined ALD/ALE sequence therefore produces periodic material accumulation and removal on both surfaces, allowing a net ASD of TiO_2 on the receptive Si−OH while avoiding substantial growth on Si−H.

XPS and Surface Topography. Deposition on the Si−OH and Si−H substrates was characterized by XPS before (i.e., N = 0) and after ALD/ALE = (30/5) × N at 170 °C, for N = 10, 14, and 18 supercycles. Figure 4a shows the Ti 2p data collected on Si−OH and Si−H surfaces, and Figure 4b shows a magnified view of the Ti 2p data on Si−H after ALD/ALE and on Si−H after ALD/ALE with additional ALE "postetch" treatment in the reactor immediately following ALD/ALE. The receptive Si−OH shows a distinct Ti−O signal for each data set. The starting Si−H surface shows no Ti 2p signal, whereas small peaks just above the XPS detection limit (visible in the expanded view data) are observed after N = 10 and 14 supercycles with no postetch. After N = 18 supercycles (i.e., after a total of 540 ALD cycles) with no postetch, the Ti 2p peak is more visible (~2 at. %). Ellipsometry analysis shows <0.15 nm after N = 10 and 14, with <1 nm of film after N = 18. From two separate tests at N = 18, one sample showed ~0.5 nm (data in Figure 2) and another showed ~0.9 nm of TiO_2. For samples with the additional postetch ALE cycles, the results in Figure 4b after N = 10 and 14 supercycles show the Ti 2p signal below the XPS detection limit (i.e., <0.6 at. %). After N = 18 supercycles, a small detectable Ti 2p signal remains present on Si−H, even after 60 postetch ALE cycles. Ellipsometry on this sample shows an oxide with thickness ~0.13 nm. This indicates that "postetch" ALE can remove some remaining TiO_2 after ALD/ALE, but the postetch is not perfectly effective at nuclei removal. At 150 °C, XPS analysis of postetching (not shown) produced similar results. As discussed below in relation to ASD selectivity loss, the material remaining on the Si−H surface after ALE is ascribed to the mixed Ti/Si oxide, which forms during the many deposition/etching cycles, where the mixed oxide nuclei do not etch as readily as TiO_2 under the ALE conditions.

Figure 4c,d shows the data for the Si 2p and W 4f binding regions, respectively, collected on Si−H and Si−OH substrates after ALD/ALE without ALE postetching. In the Si 2p region, the starting Si−H shows a feature at 99.27 eV because of Si−Si bonding, with nearly no detectable Si−O feature near 103 eV. A small positive shift of +0.52 eV for the Si−Si peak on the Si−H surface is explained by C−F bonds in the reference adventitious carbon peak after HF cleaning (Figure S3). After N = 10, 14 and 18, the Si−Si feature still dominates, with some evidence for a small Si−O signal at 103 eV. In the W 4f region, the signal near 35.4 eV is ascribed to oxidized W, and the overlapping signal is expected from Ti 3p at 37.2 eV. On the TiO_2 film on Si−OH, the Ti−O 3p peak is mainly observed at 37.2 eV, with a small W signal at 35.4 eV,[62] consistent with some W within the TiO_2 deposited layer [~0.1 at. % W for ALD/ALE = (30/5) × 8 at 170 °C].

We also used XPS to examine the surfaces after ALD/ALE for signals related to B, F, and Cl (Figure S3). The results show a noticeable signal corresponding to B (3−5 at. %) on the deposited TiO_2 on Si−OH with none detected on Si−H up to N = 18. For all samples, XPS showed nearly no detectable Cl signals after ALD/ALE. However, a small C−F signal (689 eV) and a metallic F signal (684.3−685.6 eV) were observed, ascribed to C−F bonding (at 689 eV) due to fluorination of adventitious carbon, consistent with the XPS analysis of TiO_2 after ALE.[50]

Surface topography of TiO_2 surfaces formed by ALD and by coupled ALD/ALE was also examined by scanning force imaging (Figure S4). TiO_2 films with thicknesses of 8−11 nm formed by ALD or by ALD/ALE on receptive SiO_2 both show very smooth surfaces with root-mean-squared roughness <0.2 nm, consistent with previously reports of ALD amorphous TiO_2.[56] This confirms that integrating ALE into the ALD sequence does not induce surface roughening.

Integrated TiO_2 ALD/ALE Supercycles on Patterned Si/SiO_2. The TiO_2 ALD/ALE reaction sequence was also studied on Si/SiO_2 line-pattern substrates. Figure 5 shows angle-view SEM and cross-sectional TEM images on patterned substrates for ALD only (300 cycles) and ALD/ALE = 30/5 after N = 8 and 10 supercycles at 170 °C. The SEM images were collected on as-prepared samples, without additional metal sputter-coating. Considering the ALD-only sample, SEM after 300 ALD cycles shows a smooth surface on the SiO_2 region but a relatively rough surface texture on the Si−H region. The rough surface is ascribed to preferential TiO_2 crystallization on crystalline Si−H versus amorphous SiO_2, which causes grain boundary grooving and faceting on the Si−H region.[66] The TEM cross-section in Figure 5b shows ~9.2

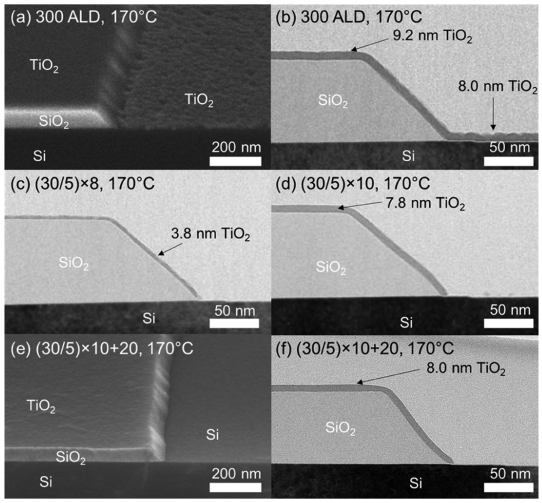

Figure 5. (a) Angled SEM and (b) cross-sectional TEM for 300 ALD cycles at 170 °C on Si/SiO_2. Cross-sectional TEM for (c) (30/5) × 8 at 170 °C on Si/SiO_2 and (d) (30/5) × 10 at 170 °C on Si/SiO_2. (e) Angled SEM and (f) cross-sectional TEM for (30/5) × 10 + 20 × ALE at 170 °C on Si/SiO_2. Note that SEM and TEM results for samples formed at 150 °C are shown in Figure 7.

DOI: 10.1021/acs.chemmater.9b01143
Chem. Mater. 2019, 31, 4793−4804

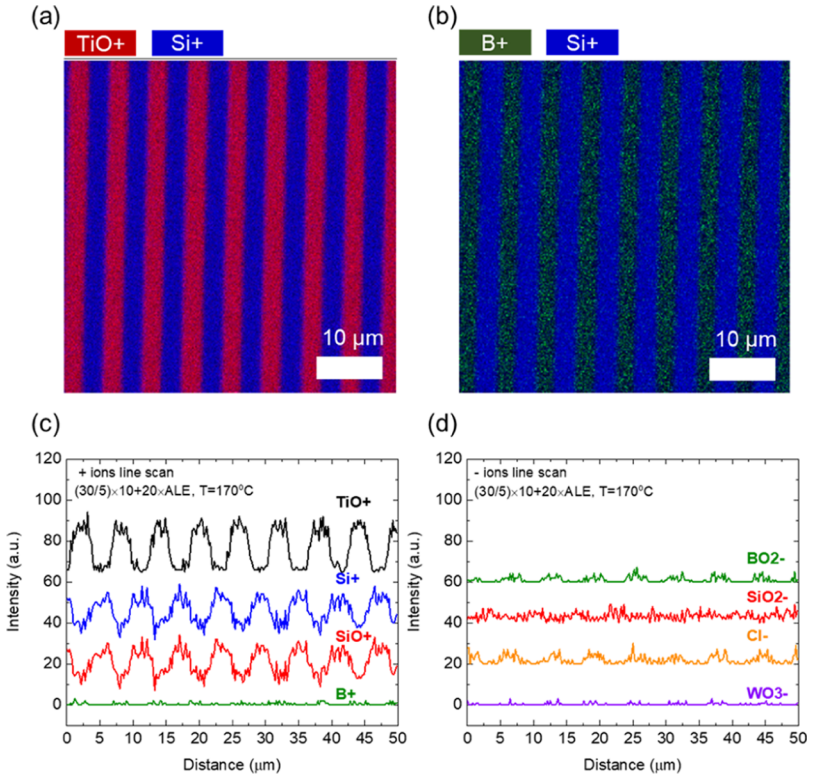

Figure 6. TOF-SIMS data collected from (30/5) × 10 + 20 × ALE at 170 °C on the Si/SiO_2 pattern. 2D element mapping (50 × 50 μm^2) of (a) TiO^+ and Si^+ overlay and (b) B^+ and Si^+ overlay. (c) + ions line scanning and (d) − ions line scanning of the same sample.

nm of TiO_2 on SiO_2 and a somewhat thinner layer on Si−H. The reduced thickness on Si−H is consistent with inhibited nucleation on this surface. Figure 5c shows a TEM cross-section after eight ALD/ALE supercycles, with ∼3.8 nm of TiO_2 on SiO_2 and no visible deposition on the Si−H region. After 10 ALD/ALE supercycles, Figure 5d shows 7.8 nm film deposition on the SiO_2 region and a few particles on Si−H. After 10 ALD/ALE supercycles with additional 20 ALE cycles, Figure 5e,f shows a clean Si−H surface and 8.0 nm of smooth oxide deposition only on the SiO_2 substrate region. For all patterned samples analyzed by TEM, TiO_2 thickness on SiO_2 is found to be less than that measured by ellipsometry on blanket samples prepared under the same conditions. This is ascribed to a small inhibition in TiO_2 nucleation on the patterned SiO_2, possibly due to surface impurities remaining after photolithography and surface cleaning, which will likely be different for different samples. Even so, the trends observed in the Si−H surface on the patterned wafers match well with the trends observed on the blanket Si−H.

A patterned sample from the same run as that in Figure 5e,f (i.e., ALD/ALE = (30/5) × 10 + 20 × ALE at 170 °C) was analyzed by TOF-SIMS. Figure 6 shows the elemental mapping of TiO^+/Si^+ and B^+/Si^+ in panels (a) and (b), respectively, and the corresponding line-scans for positive and negative ions in panels (c) and (d), respectively. All line-scans are plotted on the same *y*-axis scale but are off-set for clarity. The blue regions in Figure 6a,b represent Si^+ ions, red corresponds to TiO^+, and green represents the B^+ signal. The width of the patterns is consistent with the starting SiO_2/Si−H surfaces. The line-scans in Figure 6c,d show a small signal related to B^+ and trace B^-, Cl^-, and W^-, all coinciding with the TiO_2 region, consistent with the XPS results in Figure S3. Also, in Figure 6c, the TiO^+ signal in the Si−H region is at or below the detection limit, also consistent with XPS.

Additional Considerations. *Detection and Analysis of ASD Selectivity Loss.* For the integrated ALD/ALE process conditions used, analysis by XPS, TEM, SEM, and TOF-SIMS in Figures 4−6 shows good selectivity using 10 ALD/ALE supercycles. To explore the limits of this process, we prepared samples on patterned Si/SiO_2 substrates using N = 12 and 14 supercycles at 150 °C and analyzed results by TEM, SEM, and energy-dispersive X-ray spectroscopy (EDX). TEM and SEM are shown in Figure 7, and EDX is given in Figure S5. From the TEM images, it can be seen that 12 and 14 supercycles at 150 °C produce smooth TiO_2 with thicknesses ∼8.7 and 11.8 nm on SiO_2, but some particles are visible on the adjacent Si−H surface. XPS analysis of Si−H samples prepared under the same conditions (Figure S6) shows a small visible Ti 2p signal

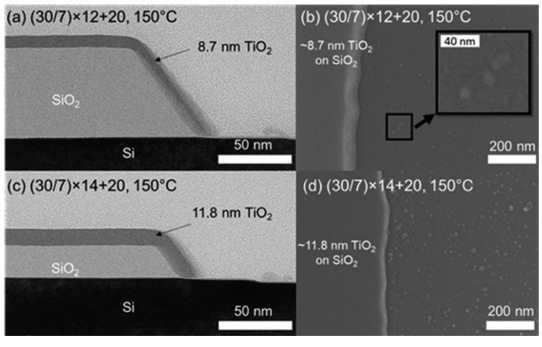

Figure 7. TEM (left) and SEM (right) results for TiO_2 ALD/ALE at 150 °C on patterned Si/SiO_2. Top row: (ALD/ALE) × N = (30/7) × 12 + 20 × ALE. Bottom row: (30/7) × 14 + 20 × ALE.

DOI: 10.1021/acs.chemmater.9b01143
Chem. Mater. 2019, 31, 4793−4804

and some silicon oxidation. Top-view SEM images are also included, more clearly showing particles on the Si−H region, indicating some unwanted growth and loss of selectivity. The particles are small (≲10 nm diameter) for the N = 12 sample, as indicated in the magnified SEM inset in Figure 7b. Note that in the inset figure, after a total of 360 ALD cycles, the surface shows ∼4 particles in an area of 100 × 100 nm^2 or 4 × 10^{-4} particles/nm^2. Under the conditions used, the N = 14 sample shows somewhat larger particles and particle density, consistent generation of nucleation sites, and continued particle growth between N = 12 and 14. Generation of nucleation sites is consistent with the data and model fit shown in Figure 2b and discussed above. When the EDX analysis is focused onto the SiO_2 substrate region, a strong Ti signal is observed, consistent with TiO_2 on SiO_2. However, focusing EDX in the particle region (Figure S5) shows no detectable Ti signal. The deep X-ray penetration depth in EDX results in relatively poor surface elemental detection,[67] but the lack of Ti signal is consistent with the particles partially containing SiO_2, in agreement with the XPS results.

To further understand the selectivity loss during integrated ALD/ALE and to observe the extent and mechanisms of Si−H surface oxidation, the ALD/ALE reactions were studied by IR transmission on high-surface-area silicon wafers with Si−OH and Si−H surface terminations.[60,61] Figure 8 shows the IR transmission results in the Si−H stretching and OH bending regions for the as-formed porous Si−H and Si−OH as well as a Si−H sample after ALD/ALE = (30/5) × 8 supercycles of TiO_2 at 170 °C. Also shown is a Si−H sample after exposure to 40 cycles of ALE alone, without any ALD. The as-formed Si−OH shows coupled Si−OH stretching modes at 3200−3600 cm^{-1},[68−70] with no detectable Si−H stretching signal near 2100 cm^{-1},[60,68,69] consistent with oxidized silicon. The starting porous Si−H sample shows a distinct Si−H stretch peak and little oxidation, with flat absorption in the 3200−3600 cm^{-1} range. The Si−H samples exposed to 40 cycles of ALE only show a complete loss of Si−H and an increase in the Si−OH signal. This confirms that the WF_6/BCl_3 ALE reactants remove surface-passivating Si−H species, thereby promoting surface oxidation. Surface Si−H passivation removal by halogenated species and promotion of surface oxidation are well documented in previous studies.[71] For the Si−H sample exposed to 8 ALD/ALE supercycles (i.e., a total of 40 ALE cycles), the data also shows similar loss of Si−H and increase in Si−OH. These results are consistent with the proposed hypothesis that the ALE sequence promotes the removal of surface passivation allowing formation of silicon oxide and/or mixed Si−Ti oxide nuclei that are less able to be removed during the ALE steps.

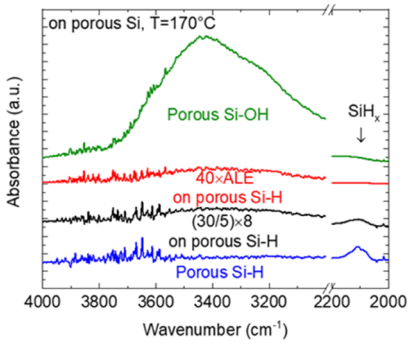

Figure 8. Transmission Fourier transform infrared absorbance peaks collected from differently treated porous silicon substrates; green line for piranha-cleaned porous silicon (porous Si−OH), red line for 40 ALE cycles at 170 °C on porous Si−H, black line for (ALD/ALE) × N = (30/5) × 8 at 170 °C on porous Si−H, and blue line for piranha and HF-cleaned porous silicon (porous Si−H).

Extended TiO_2 ALD/ALE on Si−SiO_2 leads to loss of selectivity and undesired TiO_2 deposition on the starting "nongrowth" Si−H surface. We expect that if the Si−H surface becomes partially oxidized, then the oxidized regions will be receptive to TiO_2 nucleation. The ALE reaction can remove undesired TiO_2, but it is not effective at removing SiO_2, allowing the amount of surface SiO_2 to build up on Si−H as the process progresses. Eventually the amount of TiO_2 deposited would exceed the amount removed, allowing ALD to dominate. Therefore, a possible solution to extend the selectivity could include, for example, introducing a periodic selective SiO_2 etch and surface rehydrogenation to return the favorable Si−H passivated silicon surface. In this case, however, the effect of the SiO_2 etch on the desired growth surface would also need to be considered.

Unique Aspects of Coupled ALD/ALE and Extension to Other Materials. Coupling ALD and ALE into new atomic scale processes introduces new surface/reaction combinations not present in the ALD or ALE sequences alone. For example, for the ALD/ALE supercycles shown here (e.g., Figure 3), immediately after ALD, the mass loss during the first ALE cycle is less than that measured during the second or third cycle in that supercycle. Likewise, immediately after ALE, the first ALD $TiCl_4$ dose shows less mass gain than in the second and third ALD cycles. These mechanisms may or may not extend into other ALD/ALE process combinations, but evaluating and understanding unique reactions during deposition/etching process transitions will be important.

Another important challenge for the ALD/ALE approach is the overall time needed to complete the necessary reaction steps. In this study, the reactant dosing and purging times were selected to show and evaluate process feasibility, without primary attention on the overall process duration. For results in Figure 2, the total process time for one ALD/ALE = 30/5 supercycle was approximately 53 min. Shorter times could be achieved with improved process and reactor designs, but overall faster process times will likely be needed for industrial systems.

We also note that by coupling ALE with the ALD, remnants of the etchant species can remain on the growing film surface after ALE and become incorporated into the desired deposited film. For the ALE process used here, XPS shows that the ALE reactants lead to 3−5 at. % boron and 1−2 at. % fluorine in the deposited TiO_2, with much smaller signals from tungsten or chlorine. Impurities can likely be reduced by optimizing the ALE sequence and/or by developing alternate ALE processes. However, for any ALD/ALE sequence, the composition and impurity level in ALD films will be influenced by the ALE reactants and the process used, and these impurities may or may not be important depending on the ASD material and application.

We expect that the ALD/ALE approach for ASD can also extend to other deposited materials and other deposition substrates. For each material and substrate considered, effort will be needed to identify viable and optimized process conditions, including compatible ALD and ALE reactant species, reaction temperature, reactant dosing, and number and

DOI: 10.1021/acs.chemmater.9b01143
Chem. Mater. 2019, 31, 4793−4804

ratio of ALD and ALE cycles per ALD/ALE supercycle to achieve the desired ASD product thickness and selectivity fraction. Initial studies of the TiO_2 ASD process on SiO_2 versus copper substrates, for example, show inhibition of TiO_2 nucleation on clean Cu^0 but more receptive deposition on oxidized CuO or CuO_2 surfaces. Therefore, integrating a copper oxide reduction step into the ALD/ALE sequence may help to inhibit TiO_2 growth on copper. This is expected to promote TiO_2 ASD on Cu/SiO_2 surfaces.

CONCLUSIONS

This work confirms that periodic thermal ALE can be successfully integrated into an isothermal ALD/ALE supercycle scheme at 150−190 °C to enable ASD of TiO_2 on clean SiO_2 versus Si−H surfaces. Results from ellipsometry, XPS, SEM, TEM, TOF-SIMS, and associated nucleation modeling confirm that at 170 °C, this approach enables ASD of TiO_2 with thickness > 10 nm and selectivity fraction > 0.9 on patterned $Si-H/SiO_2$ substrates, the best reported ASD for a dielectric on a dielectric without the use of organic nucleation inhibitors. On Si−H surfaces, the inherent delay in TiO_2 ALD nucleation observed using $TiCl_4/H_2O$ is used to identify ALD/ALE cycle combinations that achieve net positive deposition on receptive hydroxylated silicon while removing nuclei formed on Si−H. At 170 °C, on Si−OH and Si−H substrates, 14 supercycles consisting of 30/5 ALD/ALE cycles, respectively, allowed ∼12 nm of TiO_2 deposition on oxidized silicon as measured by ellipsometry, whereas on Si−H, the XPS Ti 2p signal nears the detection limit. The Ti 2p signal decreased and became undetectable by applying 20 cycles of ALE postetch (i.e., <2 nm of TiO_2 etching) immediately after the ALD/ALE sequence. Likewise, on patterned SiO_2/Si−H surfaces, TEM images after 10 supercycles showed 8 nm of TiO_2 on Si−OH with no particles visible on Si−H by TEM or SEM. The TiO_2 thickness measured by TEM on the patterned samples is somewhat less than that measured by ellipsometry on blanket SiO_2, likely due to impurities that inhibit initial growth on the patterned SiO_2 surface. For the ALD conditions used, the extent of water dosing per cycle is larger than necessary for saturated deposition, and this excess water likely helps promote oxidation of the Si−H surface and subsequent unwanted TiO_2 deposition. We expect therefore that further optimization of the deposition and etching conditions could enable improved selectivity beyond that shown here.

We also point out several challenges to full integration of ALD and ALE, including understanding the transition from deposition to etching (and etching to deposition) as well as the problem of overall long process times.

In addition to demonstrating conditions for good selectivity, the process was extended to larger numbers of supercycles to examine trends and mechanisms associated with selectivity loss. At 170 °C, 18 supercycles produce ∼1 nm of TiO_2 on Si−H samples as measured by ellipsometry. At 150 °C, TEM images of patterned SiO_2/Si−H after 12 and 14 supercycles with postetch shows ∼8.7 and 11.8 nm of TiO_2 with visible particles on adjacent Si−H regions. XPS analysis of Si−H samples prepared under the same conditions shows small detectable signals from surface Ti−O and Si−O. SEM images of patterned samples under the same conditions show larger particles and particle density after more supercycles. This particle density increase is consistent with model fits to the ellipsometry data.

To further identify the mechanisms for selectivity loss, IR analysis was used to examine the extent of hydrogen passivation on the Si−H surface after ALD/ALE supercycles and after ALE treatment only. In both cases, the Si−H stretching vibrations from the surface hydrogen passivation is diminished by exposure to the halogenated reactants during the ALE reaction cycle. Based on this data and the XPS results on similarly prepared samples, we conclude that the nuclei observed after extended ALD/ALE cycles under constant conditions result from unwanted silicon oxidation and that small regions of surface oxide allow deposition of TiO_2 and likely formation of mixed silicon/titanium oxide particles, which are not removed by the ALE reaction step. Further adjustment and optimization of the ALD/ALE conditions and/or integration of periodic selective silicon oxide etching could further improve the overall selectivity.

ASSOCIATED CONTENT

Supporting Information

The Supporting Information is available free of charge on the ACS Publications website at DOI: 10.1021/acs.chemmater.9b01143.

More characterization data by ellipsometry, QCM, XPS, AFM, and EDX (PDF)

AUTHOR INFORMATION

Corresponding Author

*E-mail: gnp@ncsu.edu.

ORCID

Seung Keun Song: 0000-0002-2214-449X

Gregory N. Parsons: 0000-0002-0048-5859

Notes

The authors declare no competing financial interest.

ACKNOWLEDGMENTS

The authors acknowledge funding from the Semiconductor Research Corporation, Task 2729.001 and the U.S. National Science Foundation, award no. 1704151. Part of this work was performed at the Analytical Instrumentation Facility (AIF) at the North Carolina State University, which is supported by the State of North Carolina and the National Science Foundation (award number ECCS-1542015). The AIF is a member of the North Carolina Research Triangle Nanotechnology Network (RTNN), a site in the National Nanotechnology Coordinated Infrastructure (NNCI).

REFERENCES

(1) Radamson, H. H.; Kolahdouz, M. Selective Epitaxy Growth of $Si1-_xGe_x$ Layers for MOSFETs and FinFETs. *J. Mater. Sci.: Mater. Electron.* **2015**, *26*, 4584−4603.

(2) Yang, C.-C.; Baumann, F.; Wang, P.-C.; Lee, S. Y.; Ma, P.; Aubuchon, J.; Edelstein, D. Dependence of Cu Electromigration Resistance on Selectively Deposited CVD Co Cap Thickness. *Microelectron. Eng.* **2013**, *106*, 214−218.

(3) Mameli, A.; Merkx, M. J. M.; Karasulu, B.; Roozeboom, F.; Kessels, W. M. M.; Mackus, A. J. M. Area-Selective Atomic Layer Deposition of SiO_2 Using Acetylacetone as a Chemoselective Inhibitor in an ABC-Type Cycle. *ACS Nano* **2017**, *11*, 9303−9311.

(4) Minaye Hashemi, F. S.; Prasittichai, C.; Bent, S. F. Self-Correcting Process for High Quality Patterning by Atomic Layer Deposition. *ACS Nano* **2015**, *9*, 8710−8717.

DOI: 10.1021/acs.chemmater.9b01143
Chem. Mater. 2019, 31, 4793−4804

(5) Mackus, A. J. M.; Bol, A. A.; Kessels, W. M. M. The Use of Atomic Layer Deposition in Advanced Nanopatterning. *Nanoscale* **2014**, *6*, 10941−10960.
(6) Mackus, A. J. M.; Merkx, M. J. M.; Kessels, W. M. M. From the Bottom-Up: Toward Area-Selective Atomic Layer Deposition with High Selectivity. *Chem. Mater.* **2019**, *31*, 2−12.
(7) Closser, R. G.; Bergsman, D. S.; Ruelas, L.; Hashemi, F. S. M.; Bent, S. F. Correcting Defects in Area Selective Molecular Layer Deposition. *J. Vac. Sci. Technol., A* **2017**, *35*, 031509.
(8) Parsons, G. N. Functional Model for Analysis of ALD Nucleation and Quantification of Area-Selective Deposition. *J. Vac. Sci. Technol., A* **2019**, *37*, 020911.
(9) Xie, J.; Yang, X.; Han, B.; Shao-Horn, Y.; Wang, D. Site-Selective Deposition of Twinned Platinum Nanoparticles on $TiSi_2$ Nanonets by Atomic Layer Deposition and Their Oxygen Reduction Activities. *ACS Nano* **2013**, *7*, 6337−6345.
(10) Kim, W.-H.; Minaye Hashemi, F. S.; Mackus, A. J. M.; Singh, J.; Kim, Y.; Bobb-Semple, D.; Fan, Y.; Kaufman-Osborn, T.; Godet, L.; Bent, S. F. A Process for Topographically Selective Deposition on 3D Nanostructures by Ion Implantation. *ACS Nano* **2016**, *10*, 4451−4458.
(11) Bobb-Semple, D.; Nardi, K. L.; Draeger, N.; Hausmann, D. M.; Bent, S. F. Area Selective Atomic Layer Deposition Assisted by Self-Assembled Monolayers: A Comparison of Cu, Co, W and Ru. *Chem. Mater.* **2019**, *31*, 1635−1645.
(12) Longo, R. C.; McDonnell, S.; Dick, D.; Wallace, R. M.; Chabal, Y. J.; Owen, J. H. G.; Ballard, J. B.; Randall, J. N.; Cho, K. Selectivity of Metal Oxide Atomic Layer Deposition on Hydrogen Terminated and Oxidized Si(001)-(2×1) Surface. *J. Vac. Sci. Technol., B: Microelectron. Nanometer Struct.–Process., Meas., Phenom.* **2014**, *32*, 03D112.
(13) Kalanyan, B.; Lemaire, P. C.; Atanasov, S. E.; Ritz, M. J.; Parsons, G. N. Using Hydrogen to Expand the Inherent Substrate Selectivity Window during Tungsten Atomic Layer Deposition. *Chem. Mater.* **2016**, *28*, 117−126.
(14) Tao, Q.; Overhage, K.; Jursich, G.; Takoudis, C. On the Initial Growth of Atomic Layer Deposited TiO_2 films on Silicon and Copper Surfaces. *Thin Solid Films* **2012**, *520*, 6752−6756.
(15) Lemaire, P. C.; King, M.; Parsons, G. N. Understanding Inherent Substrate Selectivity during Atomic Layer Deposition: Effect of Surface Preparation, Hydroxyl Density, and Metal Oxide Composition on Nucleation Mechanisms during Tungsten ALD. *J. Chem. Phys.* **2017**, *146*, 052811.
(16) Singh, J. A.; Thissen, N. F. W.; Kim, W.-H.; Johnson, H.; Kessels, W. M. M.; Bol, A. A.; Bent, S. F.; MacKus, A. J. M. Area-Selective Atomic Layer Deposition of Metal Oxides on Noble Metals through Catalytic Oxygen Activation. *Chem. Mater.* **2018**, *30*, 663−670.
(17) Vallat, R.; Gassilloud, R.; Eychenne, B.; Vallée, C. Selective Deposition of Ta_2O_5 by Adding Plasma Etching Super-Cycles in Plasma Enhanced Atomic Layer Deposition Steps. *J. Vac. Sci. Technol., A* **2017**, *35*, 01B104.
(18) McDonnell, S.; Longo, R. C.; Seitz, O.; Ballard, J. B.; Mordi, G.; Dick, D.; Owen, J. H. G.; Randall, J. N.; Kim, J.; Chabal, Y. J.; Cho, K.; Wallace, R. M. Controlling the Atomic Layer Deposition of Titanium Dioxide on Silicon: Dependence on Surface Termination. *J. Phys. Chem. C* **2013**, *117*, 20250−20259.
(19) Atanasov, S. E.; Kalanyan, B.; Parsons, G. N. Inherent Substrate-Dependent Growth Initiation and Selective-Area Atomic Layer Deposition of TiO_2 Using "Water-Free" Metal-Halide/Metal Alkoxide Reactants. *J. Vac. Sci. Technol., A* **2016**, *34*, 01A148.
(20) Clark, R.; Tapily, K.; Yu, K.-H.; Hakamata, T.; Consiglio, S.; O'Meara, D.; Wajda, C.; Smith, J.; Leusink, G. Perspective: New Process Technologies Required for Future Devices and Scaling. *APL Mater.* **2018**, *6*, 058203.
(21) Finnie, K. S.; Triani, G.; Short, K. T.; Mitchell, D. R. G.; Attard, D. J.; Bartlett, J. R.; Barbé, C. J. Influence of Si(100) Surface Pretreatment on the Morphology of TiO_2 Films Grown by Atomic Layer Deposition. *Thin Solid Films* **2003**, *440*, 109−116.
(22) Methaapanon, R.; Bent, S. F. Comparative Study of Titanium Dioxide Atomic Layer Deposition on Silicon Dioxide and Hydrogen-Terminated Silicon. *J. Phys. Chem. C* **2010**, *114*, 10498−10504.
(23) Ardalan, P.; Musgrave, C. B.; Bent, S. F. Effects of Surface Functionalization on Titanium Dioxide Atomic Layer Deposition on Ge Surfaces. *ECS Trans.* **2009**, *25*, 131−139.
(24) Sinha, A.; Hess, D. W.; Henderson, C. L. A Top Surface Imaging Method Using Area Selective ALD on Chemically Amplified Polymer Photoresist Films. *Electrochem. Solid-State Lett.* **2006**, *9*, G330.
(25) Sinha, A.; Hess, D. W.; Henderson, C. L. Transport Behavior of Atomic Layer Deposition Precursors through Polymer Masking Layers: Influence on Area Selective Atomic Layer Deposition. *J. Vac. Sci. Technol., B: Microelectron. Nanometer Struct.–Process., Meas., Phenom.* **2007**, *25*, 1721.
(26) Sinha, A.; Hess, D. W.; Henderson, C. L. Area-Selective ALD of Titanium Dioxide Using Lithographically Defined Poly(Methyl Methacrylate) Films. *J. Electrochem. Soc.* **2006**, *153*, G465.
(27) Ghosal, S.; Baumann, T. F.; King, J. S.; Kucheyev, S. O.; Wang, Y.; Worsley, M. A.; Biener, J.; Bent, S. F.; Hamza, A. V. Controlling Atomic Layer Deposition of TiO_2 in Aerogels through Surface Functionalization. *Chem. Mater.* **2009**, *21*, 1989−1992.
(28) Sinha, A.; Hess, D. W.; Henderson, C. L. Area Selective Atomic Layer Deposition of Titanium Dioxide: Effect of Precursor Chemistry. *J. Vac. Sci. Technol., B: Microelectron. Nanometer Struct.–Process., Meas., Phenom.* **2006**, *24*, 2523.
(29) Park, M. H.; Jang, Y. J.; Sung-Suh, H. M.; Sung, M. M. Selective Atomic Layer Deposition of Titanium Oxide on Patterned Self-Assembled Monolayers Formed by Microcontact Printing. *Langmuir* **2004**, *20*, 2257−2260.
(30) Seo, E. K.; Lee, J. W.; Sung-Suh, H. M.; Sung, M. M. Atomic Layer Deposition of Titanium Oxide on Self-Assembled-Monolayer-Coated Gold. *Chem. Mater.* **2004**, *16*, 1878−1883.
(31) Minaye Hashemi, F. S.; Birchansky, B. R.; Bent, S. F. Selective Deposition of Dielectrics: Limits and Advantages of Alkanethiol Blocking Agents on Metal-Dielectric Patterns. *ACS Appl. Mater. Interfaces* **2016**, *8*, 33264−33272.
(32) Hua, Y.; King, W. P.; Henderson, C. L. Nanopatterning Materials Using Area Selective Atomic Layer Deposition in Conjunction with Thermochemical Surface Modification via Heated AFM Cantilever Probe Lithography. *Microelectron. Eng.* **2008**, *85*, 934−936.
(33) Reinke, M.; Kuzminykh, Y.; Hoffmann, P. Selective Growth of Titanium Dioxide by Low-Temperature Chemical Vapor Deposition. *ACS Appl. Mater. Interfaces* **2015**, *7*, 9736−9743.
(34) Langston, M. C.; Dasgupta, N. P.; Jung, H. J.; Logar, M.; Huang, Y.; Sinclair, R.; Prinz, F. B. In Situ Cycle-by-Cycle Flash Annealing of Atomic Layer Deposited Materials. *J. Phys. Chem. C* **2012**, *116*, 24177−24183.
(35) Huang, J.; Lee, M.; Lucero, A.; Cheng, L.; Kim, J. Area-Selective ALD of TiO_2 Nanolines with Electron-Beam Lithography. *J. Phys. Chem. C* **2014**, *118*, 23306−23312.
(36) Haider, A.; Yilmaz, M.; Deminskyi, P.; Eren, H.; Biyikli, N. Nanoscale Selective Area Atomic Layer Deposition of TiO_2 Using E-Beam Patterned Polymers. *RSC Adv.* **2016**, *6*, 106109−106119.
(37) Biyikli, N.; Haider, A.; Deminskyi, P.; Yilmaz, M. Self-Aligned Nanoscale Processing Solutions via Selective Atomic Layer Deposition of Oxide, Nitride, and Metallic Films. *Low-Dimensional Materials and Devices 2017*; International Society for Optics and Photonics: San Diego, California, 2017.
(38) Stevens, E.; Tomczak, Y.; Chan, B. T.; Altamirano Sanchez, E.; Parsons, G. N.; Delabie, A. Area-Selective Atomic Layer Deposition of TiN, TiO_2 , and HfO_2 on Silicon Nitride with Inhibition on Amorphous Carbon. *Chem. Mater.* **2018**, *30*, 3223−3232.
(39) Färm, E.; Kemell, M.; Ritala, M.; Leskelä, M. Selective-Area Atomic Layer Deposition with Microcontact Printed Self-Assembled Octadecyltrichlorosilane Monolayers as Mask Layers. *Thin Solid Films* **2008**, *517*, 972−975.

DOI: 10.1021/acs.chemmater.9b01143
Chem. Mater. 2019, 31, 4793−4804

(40) Vallat, R.; Gassilloud, R.; Salicio, O.; El Hajjam, K.; Molas, G.; Pelissier, B.; Vallée, C. Area Selective Deposition of TiO_2 by Intercalation of Plasma Etching Cycles in PEALD Process: A Bottom up Approach for the Simplification of 3D Integration Scheme. *J. Vac. Sci. Technol., A* **2019**, *37*, 020918.
(41) Kanarik, K. J.; Lill, T.; Hudson, E. A.; Sriraman, S.; Tan, S.; Marks, J.; Vahedi, V.; Gottscho, R. A. Overview of Atomic Layer Etching in the Semiconductor Industry. *J. Vac. Sci. Technol., A* **2015**, *33*, 020802.
(42) Carver, C. T.; Plombon, J. J.; Romero, P. E.; Suri, S.; Tronic, T. A.; Turkot, R. B. Atomic Layer Etching: An Industry Perspective. *ECS J. Solid State Sci. Technol.* **2015**, *4*, N5005−N5009.
(43) Metzler, D.; Bruce, R. L.; Engelmann, S.; Joseph, E. A.; Oehrlein, G. S. Fluorocarbon Assisted Atomic Layer Etching of SiO_2 Using Cyclic Ar/C_4F_8 Plasma. *J. Vac. Sci. Technol., A* **2014**, *32*, 020603.
(44) Oehrlein, G. S.; Metzler, D.; Li, C. Atomic Layer Etching at the Tipping Point: An Overview. *ECS J. Solid State Sci. Technol.* **2015**, *4*, N5041−N5053.
(45) Engelmann, S. U.; Bruce, R. L.; Nakamura, M.; Metzler, D.; Walton, S. G.; Joseph, E. A. Challenges of Tailoring Surface Chemistry and Plasma/Surface Interactions to Advance Atomic Layer Etching. *ECS J. Solid State Sci. Technol.* **2015**, *4*, N5054−N5060.
(46) Lee, Y.; George, S. M. Atomic Layer Etching of Al_2O_3 Using Sequential, Self-Limiting Thermal Reactions with $Sn(Acac)_2$ and Hydrogen Fluoride. *ACS Nano* **2015**, *9*, 2061−2070.
(47) Lee, Y.; Huffman, C.; George, S. M.; Lee, Y.; Huffman, C.; George, S. M. Selectivity in Thermal Atomic Layer Etching Using Sequential, Self-Limiting Fluorination and Ligand-Exchange Reactions. *Chem. Mater.* **2016**, *28*, 7657−7665.
(48) Lee, Y.; Dumont, J. W.; George, S. M. Trimethylaluminum as the Metal Precursor for the Atomic Layer Etching of Al_2O_3 Using Sequential, Self-Limiting Thermal Reactions. *Chem. Mater.* **2016**, *28*, 2994−3003.
(49) Lee, Y.; DuMont, J. W.; George, S. M. Mechanism of Thermal Al_2O_3 Atomic Layer Etching Using Sequential Reactions with $Sn(Acac)_2$ and HF. *Chem. Mater.* **2015**, *27*, 3648−3657.
(50) Lemaire, P. C.; Parsons, G. N. Thermal Selective Vapor Etching of TiO_2: Chemical Vapor Etching via WF_6 and Self-Limiting Atomic Layer Etching Using WF_6 and BCl_3. *Chem. Mater.* **2017**, *29*, 6653−6665.
(51) Xie, W.; Lemaire, P. C.; Parsons, G. N. Thermally Driven Self-Limiting Atomic Layer Etching of Metallic Tungsten Using WF_6 and O_2. *ACS Appl. Mater. Interfaces* **2018**, *10*, 9147−9154.
(52) Abdulagatov, A. I.; George, S. M. Thermal Atomic Layer Etching of Silicon Using O_2 , HF, and $Al(CH_3)_3$ as the Reactants. *Chem. Mater.* **2018**, *30*, 8465−8475.
(53) Honda, M.; Katsunuma, T.; Tabata, M.; Tsuji, A.; Oishi, T.; Hisamatsu, T.; Ogawa, S.; Kihara, Y. Benefits of Atomic-Level Processing by Quasi-ALE and ALD Technique. *J. Phys. D: Appl. Phys.* **2017**, *50*, 234002.
(54) Ishikawa, K.; Karahashi, K.; Ichiki, T.; Chang, J. P.; George, S. M.; Kessels, W. M. M.; Lee, H. J.; Tinck, S.; Um, J. H.; Kinoshita, K. Progress and Prospects in Nanoscale Dry Processes: How Can We Control Atomic Layer Reactions? *Jpn. J. Appl. Phys.* **2017**, *56*, 06HA02.
(55) Aarik, J.; Aidla, A.; Uustare, T.; Sammelselg, V. Morphology and Structure of TiO_2 Thin Films Grown by Atomic Layer Deposition. *J. Cryst. Growth* **1995**, *148*, 268−275.
(56) Saha, D.; Ajimsha, R. S.; Rajiv, K.; Mukherjee, C.; Gupta, M.; Misra, P.; Kukreja, L. M. Spectroscopic Ellipsometry Characterization of Amorphous and Crystalline TiO_2 Thin Films Grown by Atomic Layer Deposition at Different Temperatures. *Appl. Surf. Sci.* **2014**, *315*, 116−123.
(57) Gu, W.; Tripp, C. P. Role of Water in the Atomic Layer Deposition of TiO_2 on SiO_2. *Langmuir* **2005**, *21*, 211−216.
(58) Aarik, J.; Aidla, A.; Mändar, H.; Sammelselg, V. Anomalous Effect of Temperature on Atomic Layer Deposition of Titanium Dioxide. *J. Cryst. Growth* **2000**, *220*, 531−537.
(59) Ritala, M.; Leskelä, M.; Nykänen, E.; Soininen, P.; Niinistö, L. Growth of Titanium Dioxide Thin Films by Atomic Layer Epitaxy. *Thin Solid Films* **1993**, *225*, 288−295.
(60) Gupta, P.; Colvin, V. L.; George, S. M. Hydrogen Desorption Kinetics from Monohydride and Dihydride Species on Silicon Surfaces. *Phys. Rev. B* **1988**, *37*, 8234−8243.
(61) Losic, D.; Santos, A. *Electrochemically Engineered Nanoporous Materials: Methods, Properties and Applications*; Springer Series in Materials Science; Springer International Publishing Switzerland, 2015, Vol. *220*; pp 1−58.
(62) Wagner, C. D.; Riggs, W. M.; Davis, L. E.; Moulder, J. F. *Handbook of X-Ray Photoelectron Spectroscopy*; Chastain, J., Ed.; Perkin-Elmer Corporation Physical Electronics Division: USA, 1992.
(63) Sammelselg, V.; Rosental, A.; Tarre, A.; Niinistö, L.; Heiskanen, K.; Ilmonen, K.; Johansson, L.-S.; Uustare, T. TiO_2 Thin Films by Atomic Layer Deposition: A Case of Uneven Growth at Low Temperature. *Appl. Surf. Sci.* **1998**, *134*, 78−86.
(64) Dendooven, J.; Pulinthanathu Sree, S.; De Keyser, K.; Deduytsche, D.; Martens, J. A.; Ludwig, K. F.; Detavernier, C. In Situ X-Ray Fluorescence Measurements during Atomic Layer Deposition: Nucleation and Growth of TiO_2 on Planar Substrates and in Nanoporous Films. *J. Phys. Chem. C* **2011**, *115*, 6605−6610.
(65) Matero, R.; Rahtu, A.; Ritala, M. In Situ Quadrupole Mass Spectrometry and Quartz Crystal Microbalance Studies on the Atomic Layer Deposition of Titanium Dioxide from Titanium Tetrachloride and Water. *Chem. Mater.* **2001**, *13*, 4506−4511.
(66) Mitchell, D. R. G.; Attard, D. J.; Triani, G. Transmission Electron Microscopy Studies of Atomic Layer Deposition TiO_2 Films Grown on Silicon. *Thin Solid Films* **2003**, *441*, 85−95.
(67) Goldstein, J. I.; Newbury, D. E.; Michael, J. R.; Ritchie, N. W. M.; Scott, J. H. J.; Joy, D. C. *Scanning Electron Microscopy and X-ray Microanalysis*, 4th ed.; Springer-Verlag New York, 2018; pp 40−53.
(68) Gupta, P.; Dillon, A. C.; Bracker, A. S.; George, S. M. FTIR Studies of H_2O and D_2O Decomposition on Porous Silicon Surfaces. *Surf. Sci.* **1991**, *245*, 360−372.
(69) Mawhinney, D. B.; Glass, J. A.; Yates, J. T. FTIR Study of the Oxidation of Porous Silicon. *J. Phys. Chem. B* **1997**, *101*, 1202−1206.
(70) Xie, Y. H.; Wilson, W. L.; Ross, F. M.; Mucha, J. A.; Fitzgerald, E. A.; MacAulay, J. M.; Harris, T. D. Luminescence and Structural Study of Porous Silicon Films. *J. Appl. Phys.* **1992**, *71*, 2403−2407.
(71) Sreejith, K.; Pillai, C. G. S. IR Study on the Effect of Chloride Ion on Porous Silicon. *Appl. Surf. Sci.* **2006**, *252*, 8399−8403.

DOI: 10.1021/acs.chemmater.9b01143
Chem. Mater. 2019, 31, 4793−4804

Supporting Information:

Integrated Isothermal Atomic Layer Deposition/Atomic Layer Etching Super-Cycles for Area-Selective Deposition of TiO_2

*Seung Keun Song, Holger Saare and Gregory N. Parsons**

Department of Chemical and Biomolecular Engineering, North Carolina State University,

Raleigh, NC 27695, USA

Supplemental Figures

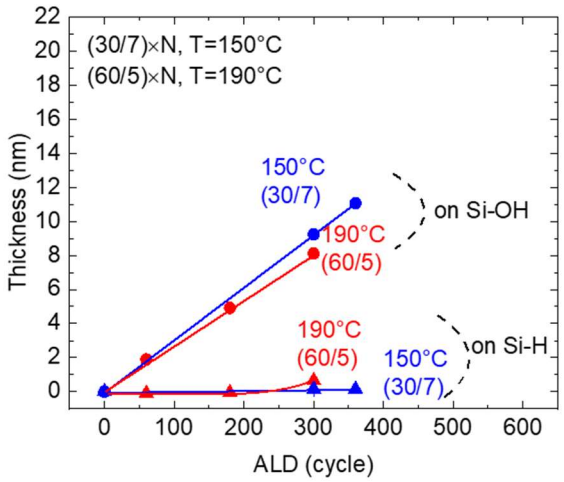

Figure S1. TiO_2 film thickness collected by ex-situ ellipsometry for ALD/ALE=(30/7)×N at 150°C, (60/5)×N at 190°C on Si-H and Si-OH substrates. These ALD/ALE cycle combinations were determined by considering growth per cycle and etch per cycle at each temperature.

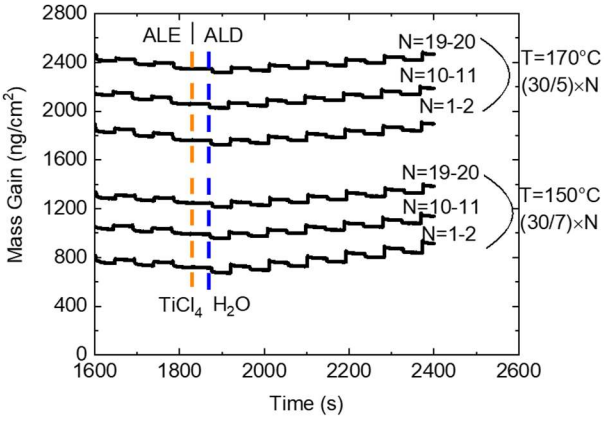

Figure S2. Expanded view of mass changes during ALE-ALD transition at different super-cycles (N=1-2, N=10-11, N=19-20) collected by in-situ QCM for (30/5)×N at 170°C and (30/7)×N at 150°C on TiO_2-coated QCM crystals. Top 3 lines are (30/5)×N at 170°C and bottom 3 lines are (30/7)×N at 150°C.

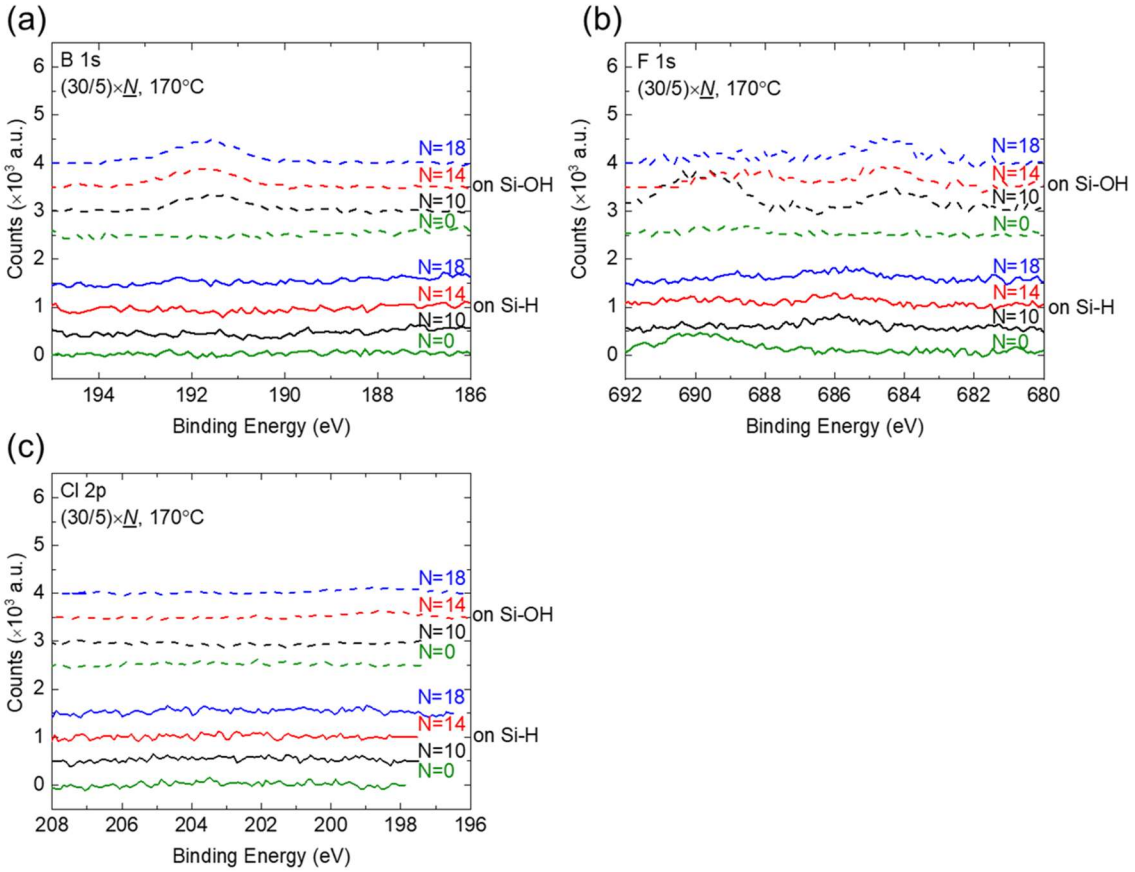

Figure S3. Ex-situ XPS (a) B 1s, (b) F 1s, and (c) Cl 2p high resolution scan for (30/5)×N at 170℃ on Si-H and Si-OH. Y-axis is magnified for easy reading. Weak Cl 2p peaks may be present for N=14, 18 in the films deposited on Si-OH.

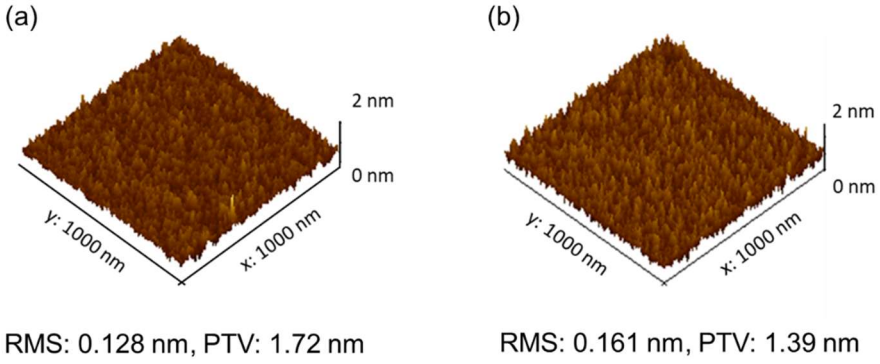

Figure S4. AFM topography images for (a) 300 TiO_2 ALD cycles at 170℃ and (b) (30/5)×10 super-cycles at 170℃ on blanket Si-OH substrates. Two kinds of roughness data for each sample are also calculated; root-mean-square (RMS) roughness, peak-to-valley (PTV) height.

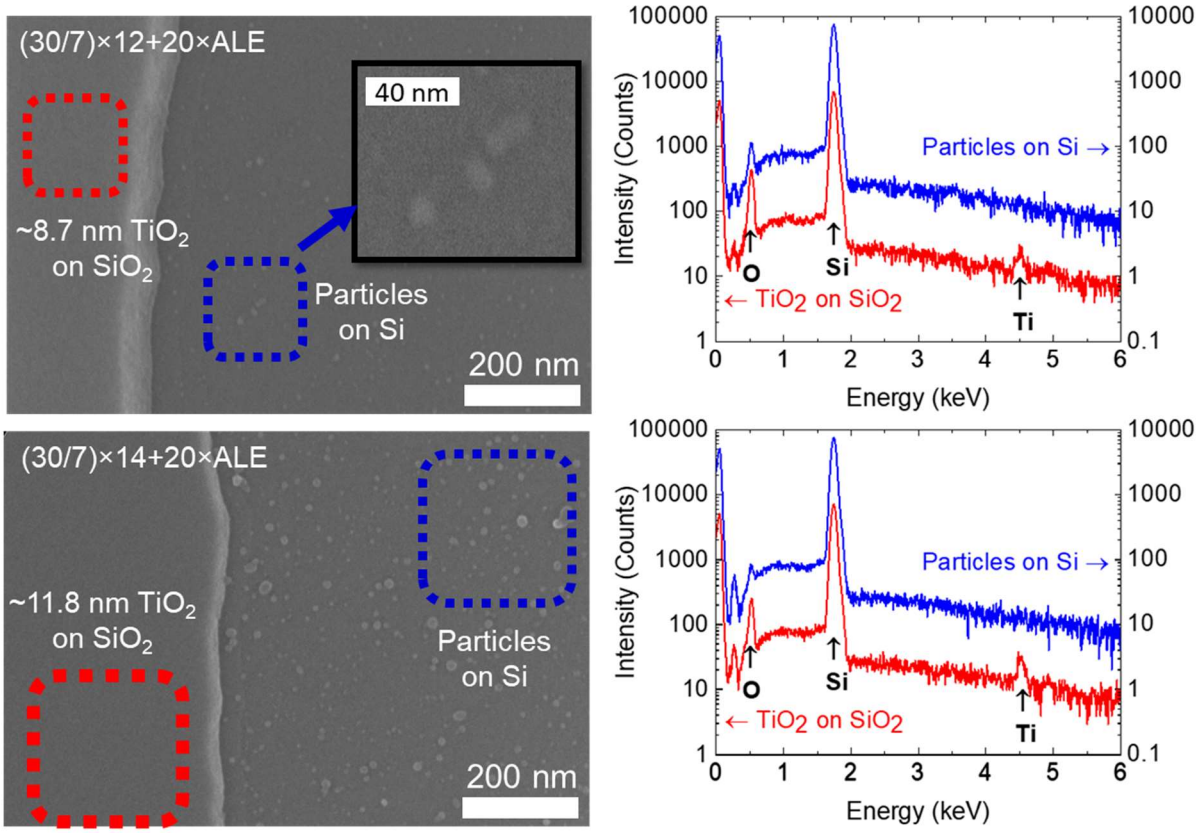

Figure S5. SEM (left) and EDX (right) results for ASD TiO_2 at 150°C on patterned Si/SiO_2. Top row: (ALD/ALE)×N =(30/7)×12+20×ALE. Bottom row: (30/7)×14+20×ALE. Particles visible on Si-H are ascribed to titanium/silicon oxide

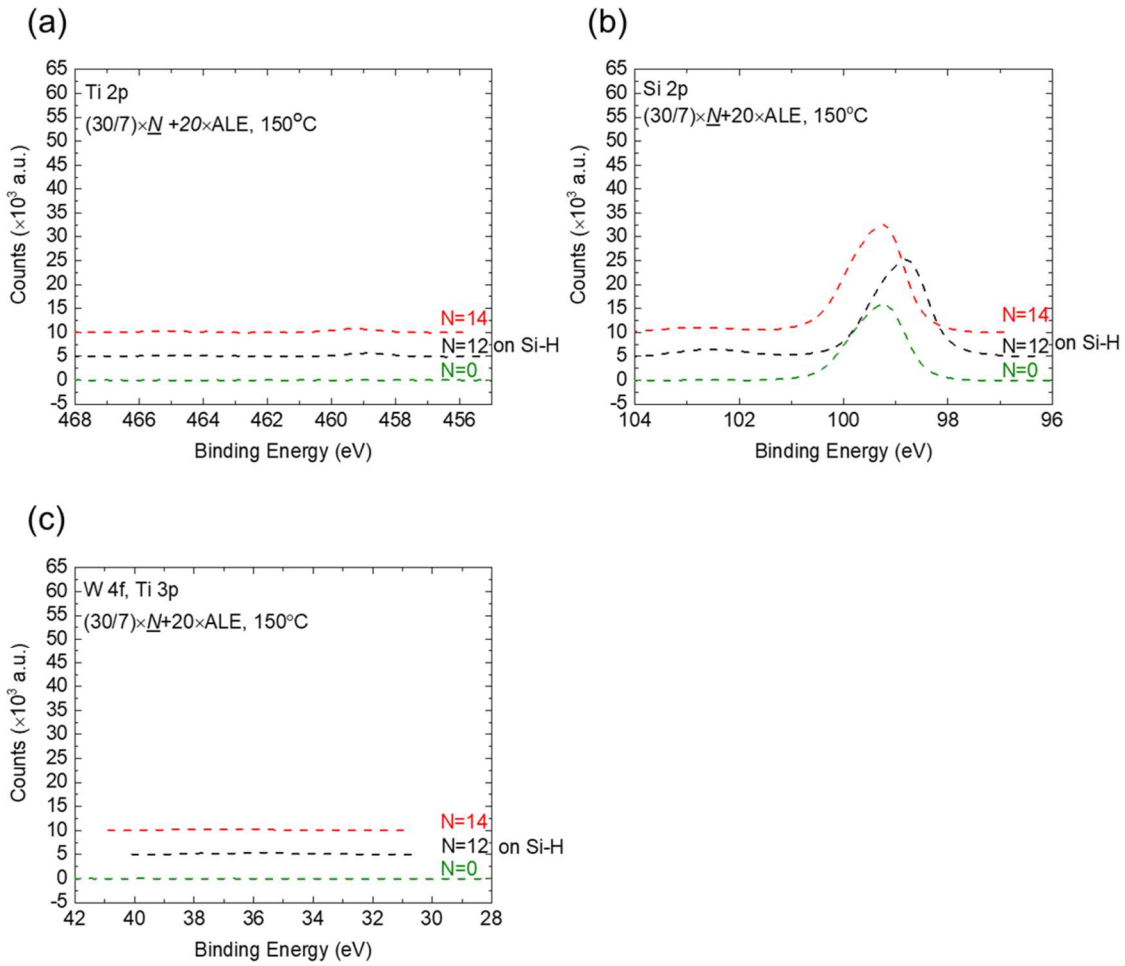

Figure S6. Ex-situ XPS (a) Ti 2p, (b) Si 2p, (c) W 4f and Ti 3p high resolution scans for (30/7)×N+20×ALE at 150°C on Si-H.